

The Chiral Induced Spin Selectivity Effect What It Is, What It Is Not, And Why It Matters

J. Fransson*[a]

Abstract: The chiral induced spin selectivity effect is an excited states phenomenon, which can be probed using photo-spectroscopy as well as transport measurements. On the one hand such measurements represent averaged quantities, on the other hand nearly all theoretical descriptions, with only a few exceptions, have been concerned with energy dependent properties of the pertinent structures. While those properties may or may not be relevant for the

chiral induced spin selectivity effect, many of those properties have been attributed as being the, or part of the, origins of the effect. Here, it is demonstrated that, for instance, the spin-resolved transmission provides little, if any, information about the chiral induced spin selectivity effect. Moreover, although effective single-electron theory can be used in this context, reasons are given for why such descriptions are not viable.

1. Introduction

Chirality is an intrinsic property of some molecules and materials, in which there is no center of inversion or mirror plane. It turns out that, when coupling such structures to the environment, for instance, spin selective processes is an emergent phenomenon^[1–3] which over the past two decades has caused an intensive debate in chemistry and physics communities about its origin.

The chiral induced spin selectivity effect has been reproducibly observed in various measurements, for instance, light exposure,^[1,2,4–18] local probing techniques,^[19–23] transport^[20,24,25] and different types of Hall measurements.^[5,6,26–28] However, although all measurements entail non-equilibrium conditions, with only a few exceptions, essentially all theoretical accounts of the effect are based on the transmission properties of chiral molecules embedded in a given environment, see for instance Refs. [29–54]. It should be mentioned that despite the concept of the transmission is not a linear response quantity in itself it is, nevertheless, in this context nearly without exception considered in linear response theory and, hence, account for only the equilibrium state properties of the molecule. Moreover, it is also often typically the result of a single particle description which under stationary condition cannot account for the excited states properties that underlie spin selectivity in chiral molecules. Finally, although the intrinsic spin-dependent properties and spin currents of chiral molecules may be interesting quantities in their own rights, see for instance Refs. [29–57], the chiral induced spin selectivity may have little, if anything, to do with those quantities.

The measurements where the chiral induced spin selectivity is observed is related to a particle flux through the molecule under two different, typically opposite, magnetic conditions. The transport set-ups, in which the charge current is under scrutiny, are intuitive in the sense that there is, at least, one electrode which can be magnetized in different

directions, see Figure 1, which thereby enables a control of the external magnetic conditions. Theoretical models to address the measured currents under such conditions have been proposed,^[16,58–70] where essentially all these various models comprise a coupling between the electronic degrees of freedom to some other, both Fermionic^[59,60,64,70] and Bosonic,^[16,61–63,65–69] degrees of freedom. Also in photospectroscopy experiments, a magnetic metal is often coupled to the sample^[8–10,12–17] and, hence, provide a control of the magnetic conditions in a similar way. The magnetic response can also be controlled using circularly polarized light.^[1,2] However, regardless of which particle flux is investigated, this flux reflects the total charge and magnetic properties of the chiral molecules, but does not provide any detailed information about its spin properties. In words pertaining to transport, the measurement concerns the charge current and nothing else.

The purpose with this article is to first discuss the theoretical framework which is relevant for the transport measurements of the chiral induced spin selectivity effect, and how this may be represented in mathematical form. Here, it is stressed that since the chiral induced spin selectivity effect is discussed in terms of the difference between the measured currents in two different set-ups, it is meaningless to compare the spin-resolved transmission, or spin-current, from a single computation with these results. It is only by considering two different set-ups, e.g., as illustrated in Figure 1, and subsequently comparing the computed transport quantities which

[a] J. Fransson

Department of Physics and Astronomy, Uppsala University, Box 516, 751 21, Uppsala, Sweden

E-mail: Jonas.Fransson@physics.uu.se

© 2022 The Authors. *Israel Journal of Chemistry* published by Wiley-VCH GmbH. This is an open access article under the terms of the Creative Commons Attribution License, which permits use, distribution and reproduction in any medium, provided the original work is properly cited.

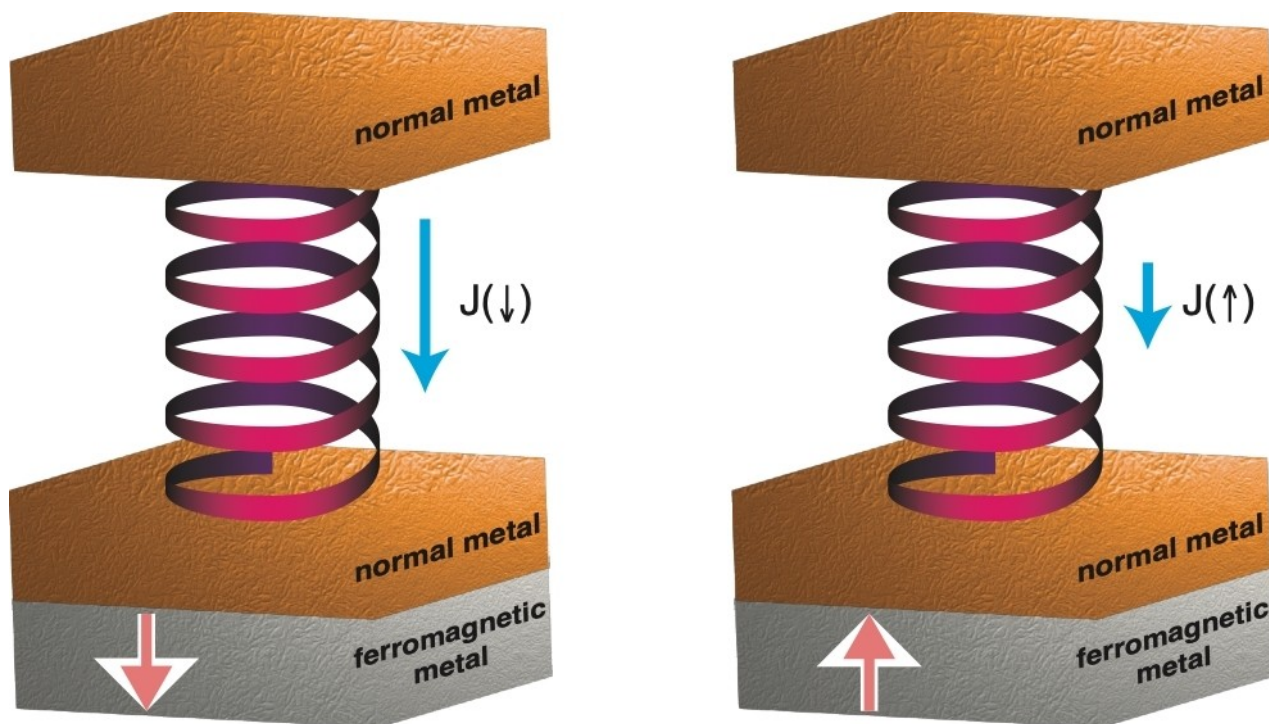


Figure 1. Schematic illustration of the transport set-up where the charge current J is measured for magnetic moment of the lower lead oriented in different directions.

represent the charge currents with each other, anything can be said about the chiral induced spin selectivity effect. Second, it is shown that the chiral induced spin selectivity can be modelled using an effective single electron description, however, such a description can only be used as a guidance for fitting since it cannot say anything about the microscopic origin of the effect.

2. Results

2.1 Transmission and Current

The first objective is to address the charge current and corresponding transmission through a molecular junction. To this end, consider a generic transport set-up, as schematically illustrated in Figure 2, where a chiral molecule is mounted in

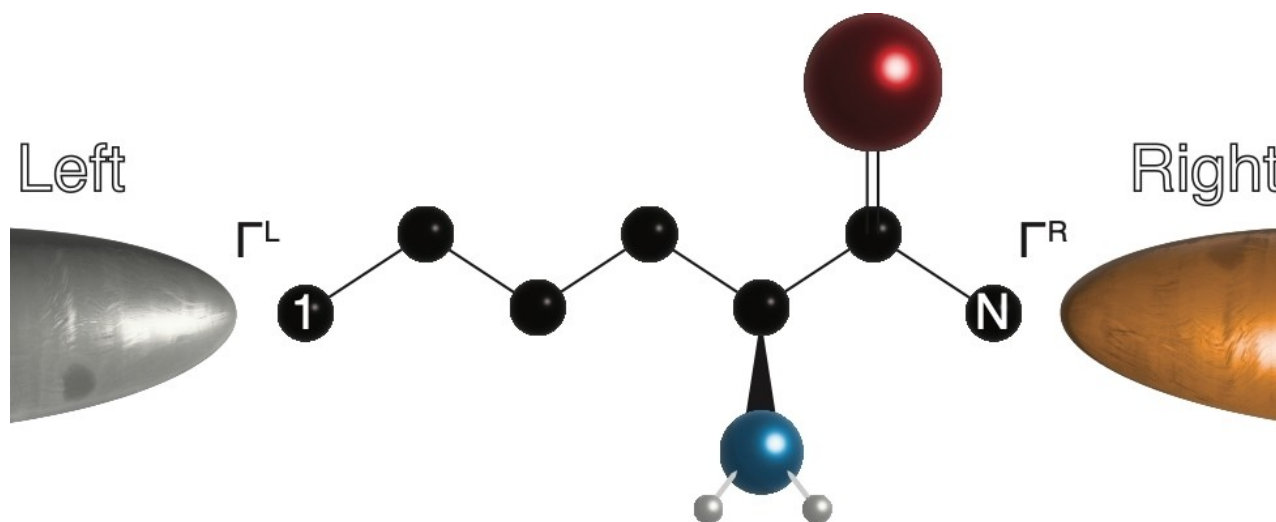


Figure 2. Schematic illustration of a chiral molecule in the junction between a ferromagnetic and normal metal.

the junction between a ferromagnetic and normal metallic lead. For the purpose of being concrete, the left lead is assumed to be ferromagnetic whereas the right is a normal metal. In the molecule, the nucleus adjacent to the left (right) lead is labelled 1 (N). All discussion henceforth is conducted under the assumption of stationary conditions, such that the charge current through the molecule can be written^[71]

$$J = \frac{ie}{h} sp \int \Gamma^L(f_L(\omega)G_1^>(\omega) + f_L(-\omega)G_1^<(\omega))d\omega. \quad (1)$$

Here, $G_1^{</>}(\omega)$ denotes the lesser/greater Green function for the site 1 which is directly coupled to the left lead with coupling strength Γ^L , whereas $f_L(\omega)$ is the Fermi-Dirac distribution function defined at the electro-chemical potential μ_L for the left lead. It should be noticed that $G_1^{</>}$ and Γ^L are a 2×2 matrices, and that the trace sp runs over spin $1/2$ space. Also, e denotes the electron charge, h is Planck's constant. Hence, the formula in Eq. (1) describes the charge current flowing across the interface between the left lead and first site in the molecule. The stationary conditions ensure current conservation such that this charge current is the same as the charge current anywhere else in the system. The non-equilibrium properties at the site 1 are given in terms of its densities of occupied ($G_1^<$) and unoccupied ($G_1^>$) electron states which, however, depend on the properties of the total system comprising the molecule and metallic leads. This is reflected through the relation $G_1^{</>} = G_{1m}^r \Sigma_{mn}^{</>} G_{n1}^a$, where the self-energy $\Sigma_{mn}^{</>}$ accounts for interactions between electrons within the molecule but also with the local environment. In the absence of internal many-body interactions, the self-energy reduces to

$$\Sigma_{mn}^{</>}(\omega) = (\pm i)\delta_{mn}(\delta_{m1}f_L(\pm\omega)\Gamma^L + \delta_{mN}f_R(\pm\omega)\Gamma^R), \quad (2)$$

which accounts for the coupling strengths Γ^χ , $\chi = L, R$, between the left (L) and right (R) leads and sites 1 and N , respectively. With these assumptions, the current can be written^[72]

$$J = \frac{e}{h} \int (f_L(\omega) - f_R(\omega))spT(\omega)d\omega, \quad (3)$$

where $T(\omega) = \Gamma^L G_{1N}^r(\omega) \Gamma^R G_{N1}^a(\omega)$ can be interpreted as the transmission matrix in the Landauer sense.

By symmetry, the transmission T can always be partitioned according to $T = T_0\sigma^0 + T_1 \cdot \sigma$, where σ^0 and σ are the identity and vector of Pauli matrices, respectively. Effecting the trace for the 2×2 -matrix T leads to that the respective charge (scalar T_0) and spin (vector $T_1 = (T_x, T_y, T_z)$) components can be defined by $T_0 = spT/2$ and $T_1 = sp\sigma T_1/2$. Here, a scalar product between a vector \mathbf{W} and σ should be read as $\mathbf{W} \cdot \sigma = W_x\sigma^x + W_y\sigma^y + W_z\sigma^z$. In the present discussion, the transmissions can be explicitly obtained in terms of the

electronic structure by putting $\mathbf{A} = G_{1N}^r$ and $\mathbf{B} = G_{N1}^a$, hence, $\mathbf{B}^\dagger = \mathbf{A}$. It is, furthermore, assumed that the left lead is ferromagnetic, $\Gamma^L = \Gamma_0(\sigma^0 + \mathbf{p}_L \cdot \sigma)/4$, where the vector \mathbf{p}_L parametrizes the orientation of the magnetic moment in the left lead such that $p_L = |\mathbf{p}_L| \leq 1$, whereas the right lead is a non-magnetic metal, $\Gamma^R = \Gamma_0\sigma^0/4$. It is convenient to decompose the transmissions into $T_m = \sum_{n=0,1} T_{mn}$, $m=0,1$, with

$$T_{00} = \left(\frac{\Gamma_0}{4}\right)^2 (A_0B_0 + \mathbf{A}_1 \cdot \mathbf{B}_1), \quad (4a)$$

$$T_{01} = \left(\frac{\Gamma_0}{4}\right)^2 \mathbf{p}_L \cdot (A_0\mathbf{B}_1 + \mathbf{A}_1B_0 + i\mathbf{A}_1 \times \mathbf{B}_1), \quad (4b)$$

$$T_{10} = \left(\frac{\Gamma_0}{4}\right)^2 (A_0\mathbf{B}_1 + \mathbf{A}_1B_0 + i\mathbf{A}_1 \times \mathbf{B}_1), \quad (4c)$$

$$T_{11} = \left(\frac{\Gamma_0}{4}\right)^2 (\mathbf{p}_L(A_0B_0 + \mathbf{A}_1 \cdot \mathbf{B}_1) + i\mathbf{p}_L \times (A_0\mathbf{B}_1 + \mathbf{A}_1B_0 + i\mathbf{A}_1 \times \mathbf{B}_1)) \quad (4d)$$

where A_0 (B_0) and \mathbf{A}_1 (\mathbf{B}_1) correspond to the charge and spin components of \mathbf{A} (\mathbf{B}), such that $\mathbf{A} = A_0\sigma^0 + \mathbf{A}_1 \cdot \sigma$ ($\mathbf{B} = B_0\sigma^0 + \mathbf{B}_1 \cdot \sigma$).

Since $spT = 2T_0$ and $sp\sigma T = 2T_1$, it is clear that only the components T_{0m} contribute to the total charge current $J \sim \int (f_L - f_R)spT d\omega$, whereas the components T_{1m} contribute to the spin current $J \sim \int (f_L - f_R)sp\sigma T d\omega$. This statement can be understood by considering the spin current $\mathbf{J}_s = \partial t(\mathbf{M}) = \partial t(\psi^\dagger \sigma \psi)$ in analogy with the charge current $J = -e\partial t(N) = -e\partial t(\psi^\dagger \psi)$, where ψ and ψ^\dagger define the annihilation and creation field spinor operators for the total electronic structure, whereas N and \mathbf{M} denote the corresponding charge and magnetic density operators, respectively. It can also be observed that while the spin components of the Green function and coupling matrices are explicitly included in the transmission T_0 , the total transmission included in the charge current is detached from a description in terms of a spin resolved formulation. This latter statement can be understood since the spin-resolved transmission $T_{\sigma\sigma'}$, where $\sigma, \sigma' \in \{\uparrow, \downarrow\}$, can be identified as

$$T_{\sigma\sigma'} = T_0\delta_{\sigma\sigma'} + T_1 \cdot \sigma_{\sigma\sigma'}, \quad (5)$$

comprising the component T_1 . It should be noticed that $T_{\sigma\sigma'}$ is the $\sigma\sigma'$ -matrix element of the matrix T , and that $\sigma_{\sigma\sigma'} = (\sigma_{\sigma\sigma'}^x, \sigma_{\sigma\sigma'}^y, \sigma_{\sigma\sigma'}^z)$ denotes the vector of the corresponding matrix elements of σ . Hence, despite the apparent spin-dependence of the transmission provided by the second contribution, only the first contribution is relevant for the charge current. Hence, any spin-dependent change in the transmission that can only be traced back to a corresponding change in T_1 , while T_0 remains unchanged, does not influence the charge current. Through the definition in Eq. (5) it can be seen, for instance, that $T_{\uparrow\uparrow}$ and $T_{\downarrow\downarrow}$ differ by

$$\mathcal{T}_{\uparrow\uparrow} - \mathcal{T}_{\downarrow\downarrow} = 2(\mathcal{T}_{10}^z + \mathcal{T}_{11}^z), \quad (6)$$

that is, this difference does not contribute to the charge current. The spin-resolved transmission is defined without reference to the external conditions \mathbf{p}_L and reflects the intrinsic spin properties of the molecule. Since, the chiral induced spin selectivity effect is measured as a response to the external conditions, as discussed above, the appropriate quantity to study is the *magneto-current*, that is, the difference

$$\Delta J \equiv J(\uparrow) - J(\downarrow), \quad (7)$$

where $J(\uparrow)$ ($J(\downarrow)$) denotes the charge current for \mathbf{p}_L ($-\mathbf{p}_L$), see Figure 1. From this definition one can deduce

$$\Delta J = \frac{2e}{h} \int (f_L - f_R)(\mathcal{T}_0(\uparrow) - \mathcal{T}_0(\downarrow)) d\omega, \quad (8)$$

such that the effect can be studied in terms of the transmission $\mathcal{T}_0(\sigma)$, as function of the orientation of \mathbf{p}_L . Therefore, this result very clearly illustrates that a non-vanishing spin-resolved transmission $\mathcal{T}_{\sigma\sigma'}$, in general, and the difference $\mathcal{T}_{\uparrow\uparrow} - \mathcal{T}_{\downarrow\downarrow}$, in particular, may have very little, if anything, to do with the comprehension of the chiral induced spin selectivity. It is, then, easy to conclude that the spin-resolved transmission does not represent an appropriate quantity of reference in the context of chiral induced spin selectivity. It, furthermore, means that the origin of the effect is not necessarily related to a spin-resolved transmission coefficient. While this analysis may seem obvious and trivial, investigations of the spin-resolved transmissions have, nevertheless, been the main focus in, for instance, Refs. [29–54].

2.2 Spin-Resolved Transmission

The phenomenology of chiral induced spin selectivity can be investigated using a simple effective model for a molecule embedded between two metallic leads. The model comprises a single electronic level, which represents, without loss of generality, the HOMO level under the assumption that the spacing to both HOMO- n , $n=1,2,3,\dots$, and LUMO+ n , $n=0,1,2,\dots$, is large enough for these levels to not take part in the conduction. The energy spectrum of this level, relative to the equilibrium chemical potential $\mu=0$ is represented by the matrix $\boldsymbol{\varepsilon} = \varepsilon_0 \sigma^0 + \boldsymbol{\varepsilon}_1 \cdot \boldsymbol{\sigma}$, where ε_0 and $\boldsymbol{\varepsilon}_1$ denote the average energy and local spin anisotropy. The latter energy, $\boldsymbol{\varepsilon}_1$, represents a local Zeeman splitting and spin anisotropy that may be present because of spin-orbit and many-body interactions, but also because of dissipation and coupling to external environment. However, the specific nature of the origins of this anisotropy is not defined here. It should be noticed, nonetheless, that this anisotropy is only present when the molecule is connected to the leads, that is, the molecule is assumed to be a closed shell structure when isolated from the environment and, hence, satisfies time-reversal symmetry. The

emergence of a local molecular spin anisotropy when the chiral molecule is connected to a metal, has been demonstrated both experimentally^[22,26] and theoretically.^[63,66] However, for simplicity, this anisotropy is here introduced as an effective parameter.

In the spirit of the approximation used already previously, the model for this considered configuration can be written

$$\mathcal{H} = \sum_{k \in L,R} \psi_k^\dagger \varepsilon_k \psi_k + \psi^\dagger \varepsilon \psi + \sum_{k \in L,R} (\psi_k^\dagger \mathbf{v}_k \psi + H.c.), \quad (9)$$

where ψ^\dagger (ψ) is the creation (annihilation) spinor for electrons in the molecule (second term), whereas ψ_k^\dagger (ψ_k) is the analogous operator for electrons in the left (L) and right (R) lead defined by the spectrum $\varepsilon_k = \varepsilon_k^{(0)} \sigma^0 + \varepsilon_k^{(1)} \cdot \boldsymbol{\sigma}$ (first term). The molecule and leads are connected through hybridization (last term) with rate matrix $\mathbf{v}_k = \mathbf{v}_k^{(0)} \sigma^0 + \mathbf{v}_k^{(1)} \cdot \boldsymbol{\sigma}$, such that the coupling Γ^χ , $\chi = L, R$, can be defined in terms of the electronic density ρ_k in the lead χ through $\Gamma^\chi = \sum_{k \in \chi} \mathbf{v}_k^\dagger \rho_k \mathbf{v}_k$. Under the conditions introduced previously, $\Gamma^L = \Gamma_0(\sigma^0 + \mathbf{p}_L \cdot \boldsymbol{\sigma})/4$ and $\Gamma^R = \Gamma_0 \sigma^0/4$.

For this example, the Green function for the molecular level can be written

$$\mathbf{G}^r(\omega) = \frac{(\omega - \varepsilon_0 + i\Gamma_0/4)\sigma^0 + (\varepsilon_1 - i\mathbf{p}_L\Gamma_0/8) \cdot \boldsymbol{\sigma}}{(\omega - \varepsilon_0 + i\Gamma_0/4)^2 - (\varepsilon_1 - i\mathbf{p}_L\Gamma_0/8)^2}, \quad (10)$$

Partitioning into charge, $G_0 = sp\mathbf{G}/2$, and spin, $\mathbf{G}_1 = sp\boldsymbol{\sigma}\mathbf{G}/2$, components leads to

$$G_0^r(\omega) = \frac{\omega - \varepsilon_0 + i\Gamma_0/4}{(\omega - \varepsilon_0 + i\Gamma_0/4)^2 - (\varepsilon_1 - i\mathbf{p}_L\Gamma_0/8)^2}, \quad (11a)$$

$$\mathbf{G}_1^r(\omega) = \frac{\varepsilon_1 - i\mathbf{p}_L\Gamma_0/8}{(\omega - \varepsilon_0 + i\Gamma_0/4)^2 - (\varepsilon_1 - i\mathbf{p}_L\Gamma_0/8)^2}, \quad (11b)$$

In relation to the transmission in the previous subsection, one can define $A_0 = G_0^r$ ($B_0 = G_0^a$), and $\mathbf{A}_1 = \mathbf{G}_1^r$ ($\mathbf{B}_1 = \mathbf{G}_1^a$), such that $\mathbf{A} = \mathbf{G}^r$ ($\mathbf{B} = \mathbf{G}^a$).

In these expressions, the poles $E \pm$ (zeros of the numerator; $(\omega - \varepsilon_0 + i\Gamma_0/4)^2 - (\varepsilon_1 - i\mathbf{p}_L\Gamma_0/8)^2$) can be written

$$E_{\pm} = \varepsilon_{\pm} - \frac{i}{\tau_{\pm}}, \quad (12a)$$

$$\varepsilon_{\pm} = \varepsilon_0 \pm \mathcal{R} \cos \frac{\varphi}{2}, \frac{1}{\tau_{\pm}} = \frac{\Gamma_0}{4} \pm \mathcal{R} \sin \frac{\varphi}{2}, \quad (12b)$$

where $\mathcal{R}^2 = [\varepsilon_1^2 - p_L^2(\Gamma_0/8)^2]^2 + (\varepsilon_1 \cdot \mathbf{p}_L)^2(\Gamma_0/4)^2$ and $\tan \varphi = (\varepsilon_1 \cdot \mathbf{p}_L)\Gamma_0/4[\varepsilon_1^2 - p_L^2(\Gamma_0/8)^2]$. Then, since \mathcal{R} remains invariant under $\mathbf{p}_L \rightarrow -\mathbf{p}_L$, while the phase φ is odd, the symmetry rules for the poles can be summarized as

$$\varepsilon_{\pm}(-\mathbf{p}_L) = \text{Re} E_{\pm}(-\mathbf{p}_L) = \text{Re} E_{\pm}(\mathbf{p}_L) = \varepsilon_{\pm}(\mathbf{p}_L), \quad (13a)$$

$$\frac{1}{\tau_{\pm}(-\mathbf{p}_L)} = \text{Im}E_{\pm}(-\mathbf{p}_L) = \text{Im}E_{\mp}(\mathbf{p}_L) = \frac{1}{\tau_{\mp}(\mathbf{p}_L)}. \quad (13b)$$

Hence, the level broadenings $1/\tau_{\pm}$ of the two levels are interchanged upon switching the sign of \mathbf{p}_L , see Figure 3 for an illustration of the modifications of the electronic upon changing the sign of \mathbf{p}_L . The plots in the figure illustrates the spin-resolved local density of electron states for a config-

uration parametrized by $\varepsilon_0 = -0.5$ eV, $\varepsilon_1 = 0.025\hat{z}$ eV, $\Gamma_0 = 0.05$ eV, and $\mathbf{p}_L = \pm 0.8\hat{z}$. Due to competition between the local anisotropy and the spin-polarization in the ferromagnetic lead, the local level is spin split, however, not into pure states but into linear combinations of the two spin projections, see, e.g., Eq. (11). By changing the sign of the spin-polarization in the ferromagnetic lead, a corresponding interchange the order of the local spin states. This interchange of the order of the spin-

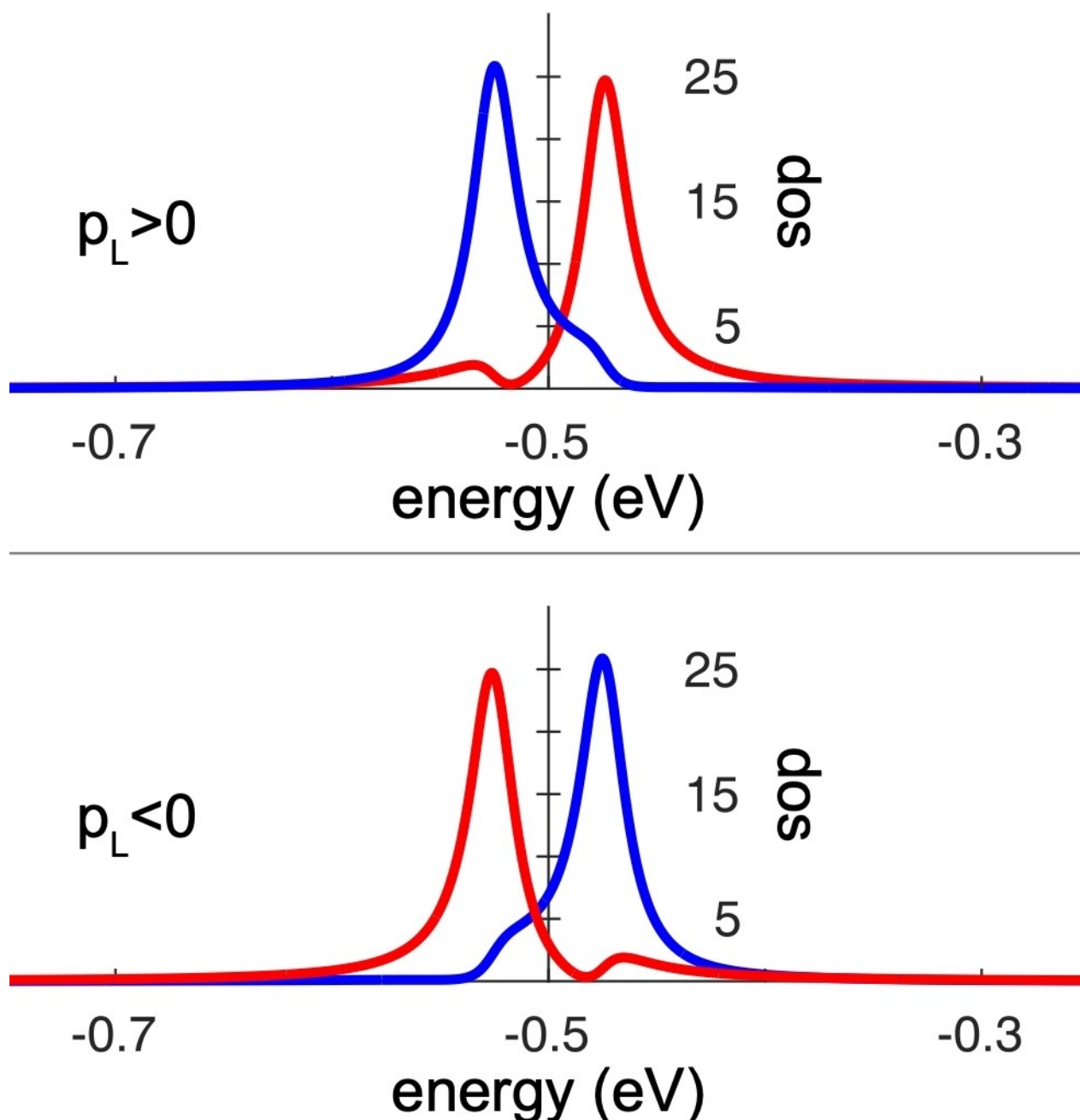


Figure 3. Example of the spin-resolved density of electron states in the molecule, using Eq. (10), for two different, opposite, spin-polarizations p_L in the left lead, indicating the interchanging level broadenings upon switching sign of p_L . The red and blue lines correspond to opposite spin projections. Here, the used parameters are $\varepsilon_0 = -0.5$ eV, $\varepsilon_1 = 0.025\hat{z}$ eV, $\Gamma_0 = 0.05$ eV, $p_L = \pm 0.8\hat{z}$.

projections does have a direct consequence on the total charge current, as will be discussed in the following.

First, consider conditions in which there is no molecular spin anisotropy, that is, $\varepsilon_1 = 0$. Then, G_0 is even with respect to the sign of \mathbf{p}_L , while G_1^x is odd, which means that the induced spin-polarization in the molecule changes sign with the sign change of \mathbf{p}_L . Moreover, under those conditions, the level broadenings $1/\tau_{\pm}$ are degenerate, since $\tan\varphi = 0$. The direct consequence of these properties is that $T_{00}(-\mathbf{p}_L) = T_{00}(\mathbf{p}_L)$, and $T_{01}(\mathbf{p}_L) \sim \mathbf{p}_L \cdot (A_0\mathbf{B}_1 + A_1\mathbf{B}_0)$ and $T_{01}(-\mathbf{p}_L) \sim -\mathbf{p}_L \cdot (-A_0\mathbf{B}_1 - A_1\mathbf{B}_0)$, such that the charge magneto-transmission $T_{01}(\mathbf{p}_L) - T_{01}(-\mathbf{p}_L)$ vanishes identically. Hence, since the total charge current is also even with respect to the sign of \mathbf{p}_L , this entails that $J(\mathbf{p}_L) - J(-\mathbf{p}_L) = 0$, that is, there is no spin selectivity effect. By contrast, since $T_{00} \neq 0$ and both T_{10} and T_{11} are odd with respect to \mathbf{p}_L , the difference $T_{00}(\uparrow) - T_{00}(\downarrow)$ is non-vanishing. Hence, despite the vanishing magneto-current, the spin-current is non-vanishing, since $T_1 \neq 0$. Also, the spin magneto-transmission $T_1(\mathbf{p}_L) - T_1(-\mathbf{p}_L) \neq 0$. This example illustrates the inappropriateness of considering the spin-resolved transmission in

the context of magneto-current studies, a conclusion that was also previously drawn in Ref. [65].

These observations are visualized in Figure 4, showing (a) the charge, $-ImG_0'/\pi$, and spin, $-ImG_1^x/\pi$, densities of states for $\mathbf{p}_L = 0.2\hat{z}$ (bold – blue color scale) and $\mathbf{p}_L = -0.2\hat{z}$ (faint – red color scale), (b) corresponding charge current (left) and normalized magneto-current, $\Delta J = 100 \cdot \Delta J / \Sigma_{\sigma} J(\sigma)$, (right), (c) transmissions, and (d) spin-resolved transmissions and magneto-transmissions. The spin-polarization \mathbf{p}_L in the left lead generates a finite spin-density in the longitudinal (\hat{z}) direction, Figure 4 (a), which changes polarity as $\mathbf{p}_L \rightarrow -\mathbf{p}_L$. This property is carried over to the transmissions T_{mn} , $m, n \in \{0, 1\}$, see Figure 4 (c), illustrating the even (odd) property of T_{0m} (T_{1m}) as $\mathbf{p}_L \rightarrow -\mathbf{p}_L$. Consequently, the spin-resolved transmission as well as spin magneto-transmission are non-vanishing, Figure 4 (d), while the charge magneto-transmission vanishes.

Second, should there be a non-vanishing molecular spin anisotropy, that is, $\varepsilon_1 \neq 0$, the over all picture changes. It may be noticed that the two components T_{00} and T_{01} can be written as

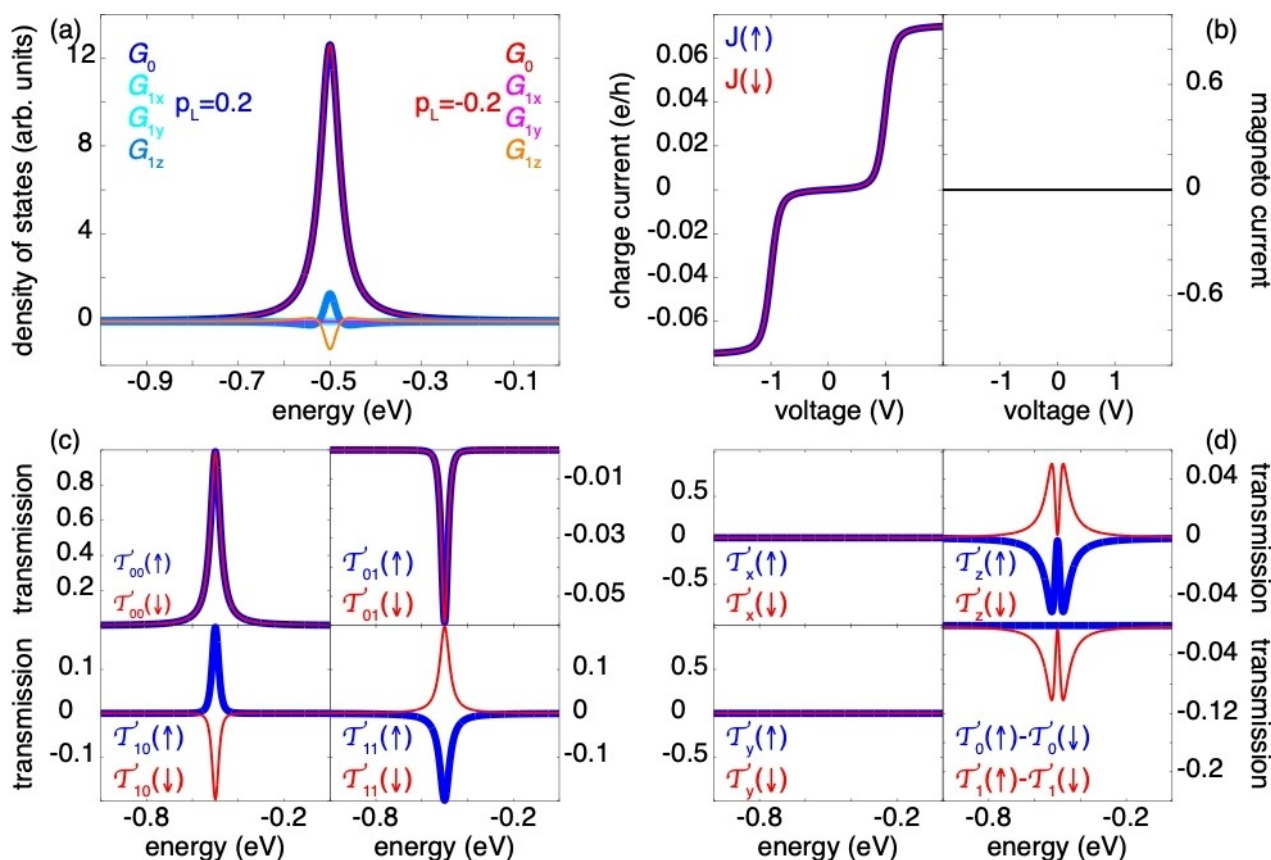


Figure 4. Single level model with vanishing spin anisotropy, $\varepsilon_1 = 0$ for $\mathbf{p}_L = 0.2\hat{z}$ (bold – blue color scale) and $\mathbf{p}_L = -0.2\hat{z}$ (faint – red color scale). (a) Charge, $-ImG_0'/\pi$, and spin, $-ImG_1^x/\pi$, resolved density of electron states. (b) Charge current (left) and normalized magneto-current (right). (c) Transmission coefficients. In the lower panels, the x- and y-components are zero (not shown). (d) Spin-resolved transmissions and magneto-transmissions. In the lower right panel, the x- and y-components of $T_1(\uparrow) - T_1(\downarrow)$ are zero (not shown). Parameters used are: $\varepsilon_0 - \mu = -0.5$ eV, $\Gamma_0 = 0.1$ eV, and $T = 300$ K.

$$T_{00} = \left(\frac{\Gamma_0}{4}\right)^2 \frac{(\omega - \varepsilon_0)^2 + \varepsilon_1^2 + (\Gamma_0/4)^2(1 + p_L^2/4)}{|(\omega - E_+)(\omega - E_-)|^2}, \quad (14a)$$

$$T_{01} = \left(\frac{\Gamma_0}{4}\right)^2 \mathbf{p}_L \cdot \frac{2\varepsilon_1(\omega - \varepsilon_0) - \mathbf{p}_L(\Gamma_0/4)^2}{|(\omega - E_+)(\omega - E_-)|^2}, \quad (14b)$$

since $\mathbf{A}_1 \times \mathbf{B}_1 \sim \mathbf{p}_L \cdot (\varepsilon_1 \times \mathbf{p}_L) = 0$. By contrast to conditions where $\varepsilon_1 = 0$, the component T_{01} is neither even nor odd with respect to the sign of \mathbf{p}_L , which is a direct consequence of the symmetry rules of the poles, see Eq. (13). Hence, the difference $T_{01}(\mathbf{p}_L) - T_{01}(-\mathbf{p}_L)$ is non-vanishing, such that also the magneto-current $\Delta J \neq 0$.

The plots in Figure 5 illustrate (a) the charge and spin densities, (b) charge and normalized magneto-current, (c) transmissions, and (d) spin-resolved transmission and magneto-transmission, for the same set-up as in the previous example, however, with $\varepsilon_1 = 25\hat{z}$ meV. The non-vanishing intrinsic local spin moment increases the separation between the spin states, which is signified by the double peak structure in the charge density. It also induces an asymmetry in the spin density, with respect to the bare level energy ε_0 . However, it

can be seen that the spin density is neither even nor odd upon sign change of \mathbf{p}_L , which leads to a finite magneto-current, see Figure 5 (b). The corresponding transmissions, Figure 5 (c), illustrate T_{00} and T_{01} , showing that the sum of their contributions is unchanged. It can also be noticed that the z-components of the transmissions T_{1m} pertaining to the spin-current carry their properties over to the spin-resolved transmissions and magneto-transmissions, see Figure 5 (d). It should also be noticed, however, that while the magneto-transmission for the charge current is asymmetric with respect to the bare energy level ε_0 , the corresponding magneto-transmission for the spin-current is symmetric. Hence, also in this situation where there is an intrinsic molecular spin anisotropy, the spin-resolved transmissions provide inappropriate information about the magneto-current.

Among the conclusions that can be drawn from these two examples, first one should notice that the spin-resolved transmission has little, if anything, to do with the mechanisms that are relevant for chiral induced spin selectivity since it is a measure for the spin current whereas chiral induced spin selectivity is measured through the magneto-current, which is

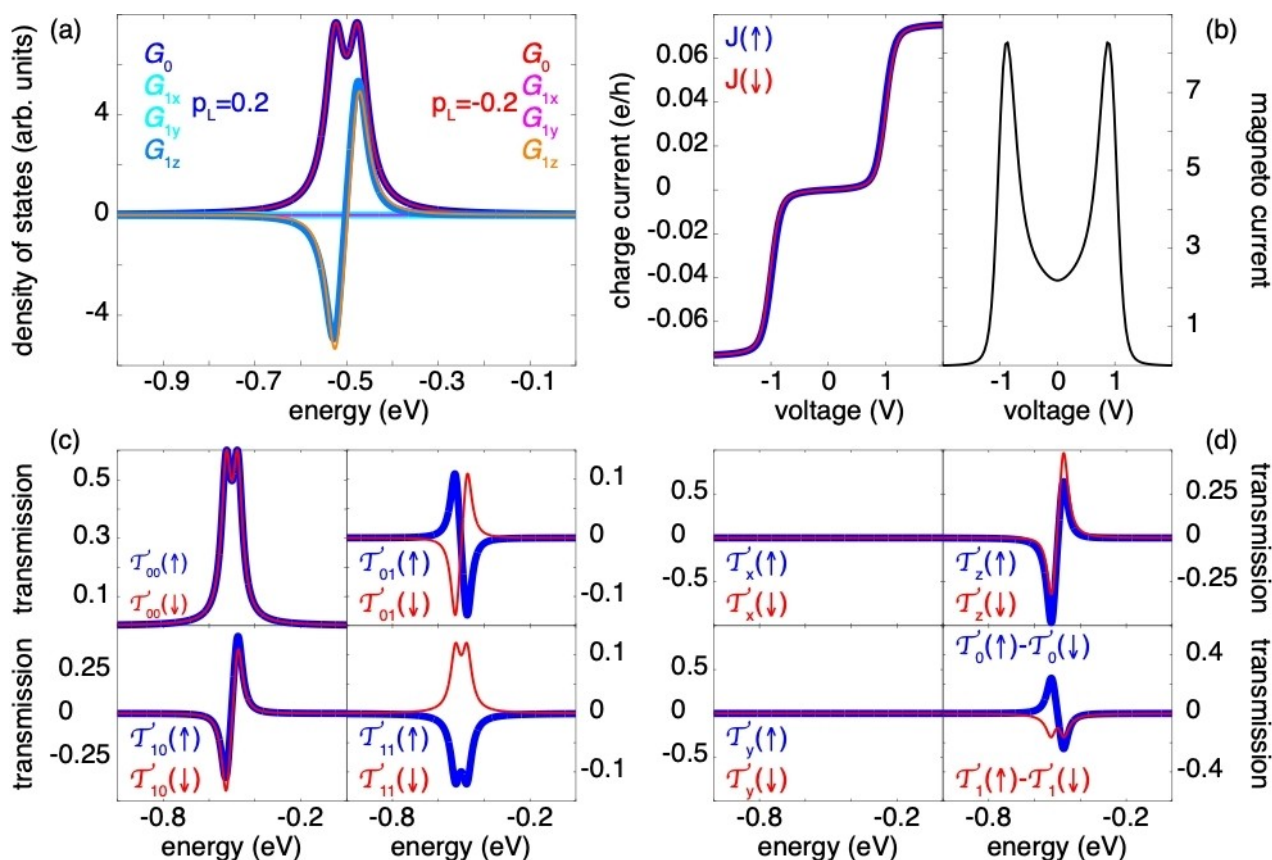


Figure 5. Single level model with non-vanishing spin anisotropy, $\varepsilon_1 = \varepsilon_1\hat{z}$, $\varepsilon_1 = 25$ meV, for $p_L = 0.2\hat{z}$ (bold – blue color scale) and $p_L = -0.2\hat{z}$ (faint – red color scale). (a) Charge, $-ImG_0/\pi$, and spin, $-ImG_1/\pi$, resolved density of electron states. (b) Charge current (left) and normalized magneto-current (right). (c) Transmission coefficients. In the lower panels, the x- and y-components are zero (not shown). (d) Spin-resolved transmissions and magneto-transmissions. In the lower right panel, the x- and y-components of $T_1(\uparrow) - T_1(\downarrow)$ are zero (not shown). Other parameters are as in Figure 4.

Research Article

the difference between two charge currents obtained in two separate measurements. However, this is not the same as to say that the spin-resolved transmission and the corresponding spin current may not be useful for the comprehension of the chiral induced spin selectivity effect. Second, a non-vanishing magneto-current can only be provided in a system comprising a component, here, the molecule, which has an intrinsic spin anisotropy, which may be absent when the molecule is isolated from the environment but exists in its presence. For instance, the magneto-current should not originate in the spin-polarized leads, since these are included for supplying a reference spin-polarization of the injected current. Hence, such leads merely play a role for the detection of the effect. Third, while an effective single-electron theory can be used to capture the phenomenon of a magneto-current, one has to include a spin anisotropy in the description which, at this simple level of description, provides a phenomenological addition for which the microscopic origin may be unknown. Fourth, the two examples illustrate that despite the transmission itself may provide sufficient information about the transport properties to predict and interpret the experimental results, it is necessary to acquire this information for all configurations considered in the experiment. Only considering the transmission without the influence of, e.g., a ferromagnetic lead or not comparing the results for the ferromagnetic lead with two opposite spin-polarizations does not allow for a full comprehension of the phenomenon.

Finally, before ending this section an issue that has been raised within the community about the properties of the spin anisotropy is addressed. It has been conjectured that the spin anisotropy ε_1 has to include a longitudinal component for the chiral induced spin selectivity effect to arise. This conjecture is, however, likely to have been made on a loose basis without a solid foundation.

Within the introduced example, it is easy to see that, e.g., a spin anisotropy $\varepsilon_1 = \varepsilon_1(\hat{x} + \hat{y})$ and spin-polarization $\mathbf{p}_L = p_L \hat{z}$ certainly leads to that the product $\varepsilon_1 \cdot \mathbf{p}_L = 0$, and that both transmissions \mathcal{T}_{0m} are even with the sign of \mathbf{p}_L . However, for a lead which is also spin-polarized in the transverse direction, that is, $\mathbf{p}_L = \mathbf{p}_\perp + p_z \hat{z}$, where $\mathbf{p}_\perp = (p_x, p_y)$ and at least one of p_x and p_y non-zero, the transmission \mathcal{T}_{01} loses its even property with the sign of \mathbf{p}_L .

In Figure 6, the results for an example with $\varepsilon_1 = \varepsilon_1(\hat{x} + \hat{y})$, $\varepsilon_1 = 25$ meV, and $\mathbf{p}_L = \pm 0.2\hat{x}$ are summarized, illustrating the non-vanishing transverse spin-polarization, (a), and corresponding magneto-current (b), as well as the transmission (c), spin-resolved transmission, and magneto-transmission (d). It is interesting to notice that despite the transverse characters of the spin-polarization and spin-anisotropy, there is, nonetheless, a non-vanishing longitudinal component to the spin magneto-transmission, see Figure 6 (d).

The conclusions of this discussion can be summarized in the following terms. First of all, in the transport set-up, the chiral induced spin selectivity effect refers to a measure of the charge currents obtained in one system under two very different conditions, or, configurations, which is outlined in

Figure 1. This picture can be generalized into some intensities $J(m)$ obtained from the same system configured under conditions, say, $m = \uparrow$ and $m = \downarrow$. The two intensities are compared through the normalized difference $\Delta J = [J(\uparrow) - J(\downarrow)]/[J(\uparrow) + J(\downarrow)]$, and should it be non-vanishing there is a measurable difference between the two configurations. As it has been made clear in this discussion, the chiral induced spin selectivity effect is *neither* a measure of the spin-polarized current *nor* is it a measure of the spin-current through the system. Hence, the transmission is a quantity which very poorly accounts for the effect, first and foremost since the effect is a result of integrated degrees of freedom whereas the transmission relates to spectral properties.

Second, the chiral induced spin selectivity effect cannot be captured in a single particle theory unless an effective spin anisotropy is included, an anisotropy that inevitable originates from the interplay between structure, spin-orbit interactions, and electron correlations. The latter picture should, therefore, be referred to as a correlated description. The difference between the descriptions is summarized by means of the schematic illustration in Figure 7. In this figure, the external conditions is represented by a ferromagnetic metal in the left lead. The presence of the ferromagnet spin splits the local molecular level. In the single particle theory, this splitting is nominally the same for both types of ferromagnets, however, with opposite signs, see panels (a), (b). The spin-polarizations of the currents in the two cases are equally strong but with the opposite signs, hence, the total charge current remains the same. In a correlated theory, there is a local spin anisotropy which competes with the influence from the ferromagnet, such that the local spin splitting is much larger in one configuration compared to the other, see panels (c), (d). This leads to a difference in the total charge current. Hence, the resulting flux through the system is *not* equal in the two configurations, since the spin anisotropy acts as an additional and *variable* resistance to the charge current between the two configurations.

2.3 Chiral Lattice Model

Next, the theoretical basis discussed in the previous section is here transferred into an effective model for chiral molecules. For the purpose of being concrete, this model is based on the lattice model introduced in Refs. [59,62,63,66] with the modifications, however, that the single electron level per site is extended to include multiple levels. Furthermore, the interactions (electron-electron or electron-vibration) that were included in those previous discussions are here replaced by a simple phenomenological spin anisotropy. The generic molecular geometry considered here is described by the set $M = M \times N$ of spatial coordinates $\mathbf{r}_m = (a \cos \varphi_m, a \sin \varphi_m, c_m)$, $\varphi_m = 2\pi(m-1)/(M-1)$, $m = 1, \dots, M$, and $c_m = c\varphi_m/2\pi$, where a and c define the radius and length, respectively, of the helical structure, where-

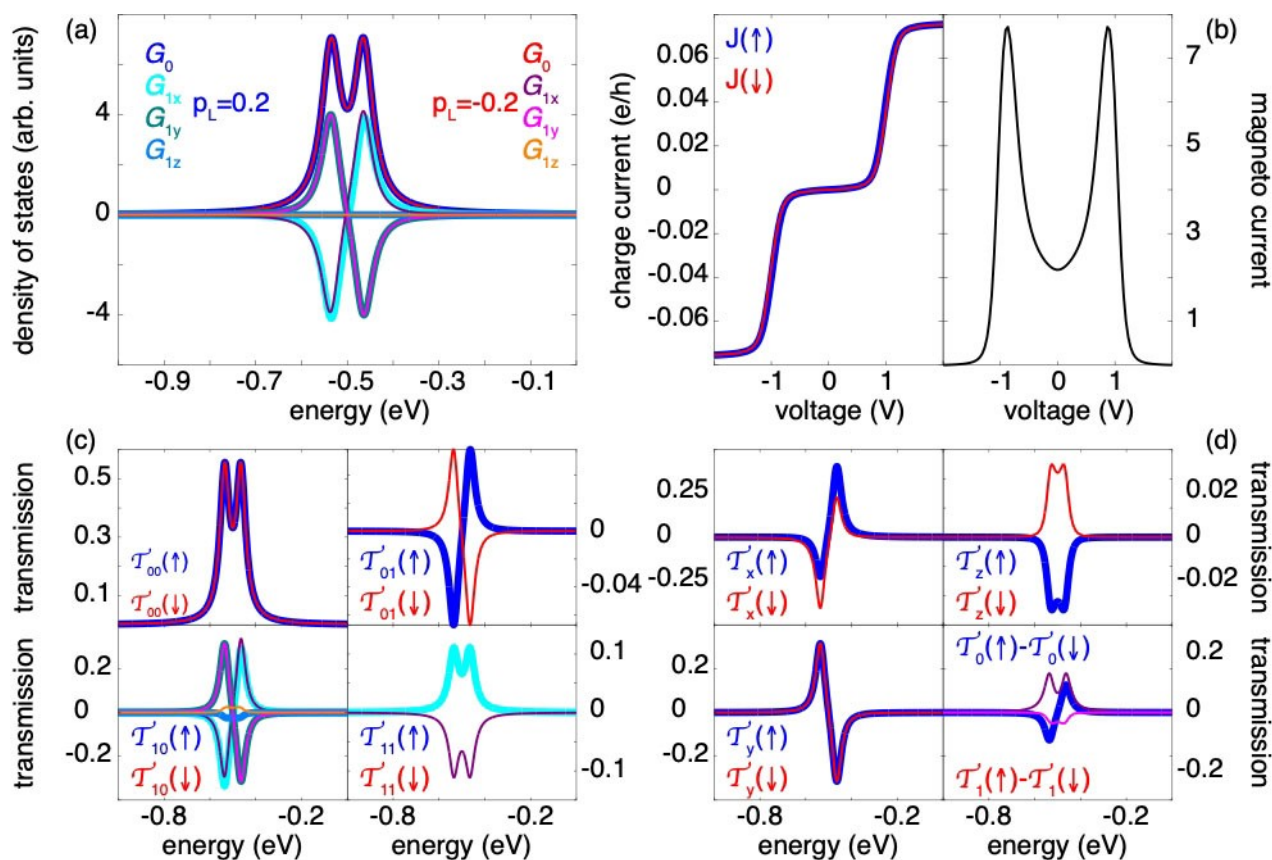


Figure 6. Single level model with non-vanishing spin anisotropy, $\varepsilon_1 = \varepsilon_1(\hat{x} + \hat{y})$, $\varepsilon_1 = 25$ meV, for $p_L = 0.2\hat{x}$ (bold – blue color scale) and $p_L = -0.2\hat{x}$ (faint – red color scale). (a) Charge, $-ImG_0(\omega)/\pi$, and spin, $-ImG_1(\omega)/\pi$, resolved density of electron states. (b) Charge current (left) and normalized magneto-current (right). (c) Transmission coefficients. In the lower left, color code is the same as in panel (a). In the lower right, the y - and z -components are zero (not shown). (d) Spin-resolved transmissions and magneto-transmissions. In the lower right, color code for $T_1(\uparrow) - T_1(\downarrow)$ is the same as in panel (a). Other parameters are as in Figure 4.

as M and N denote the number of turns and ions per turn. Each coordinate denotes an ionic site which is represented by a set of electron levels described by

$$\mathcal{H}_m = \sum_n \psi_{mn}^\dagger \varepsilon_{mn} \psi_{mn} + \sum_{nn'} (\psi_{mn}^\dagger \mathbf{w}_{mnn'} \psi_{nn'} + H.c.), \quad (15)$$

where $\psi^\dagger = (d^\dagger, a^\dagger)(\psi)$ is the creation (annihilation) spinor, $\varepsilon_{mn} = \varepsilon_{mn}^{(0)} \sigma^0 + \varepsilon_{mn}^{(1)} \cdot \sigma$ represents the bare energy spectrum for electrons in the n th level at the site, and $\mathbf{w}_{mnn'}$ denotes the matrix element for transitions between energy levels within the site.

Electrons hopping between nearest-neighboring and next nearest-neighboring sites occur with the energies $\mathbf{t}_{mnn'}$ and $i\lambda_{mnn'} \mathbf{v}_m^{(s)} \cdot \sigma$, and spin-orbit coupling is picked up between next-nearest neighbor sites through processes of the type $\psi_{mn}^\dagger \mathbf{t}_{mnn'} \psi_{(m+s)n'}$ and $i\lambda_{mnn'} \psi_{mn}^\dagger \mathbf{v}_m^{(s)} \cdot \sigma \psi_{(m+2s)n'}$, respectively, where $s = \pm 1$. Here, $\lambda_{mnn'}$ denotes the spin-orbit interaction parameter, whereas the vector $\mathbf{v}_m^{(s)} = \hat{\mathbf{d}}_{m+s} \times \hat{\mathbf{d}}_{m+2s}$ defines the chirality of the helical molecule in terms of the unit vectors

$\hat{\mathbf{d}}_{m+s} = (\mathbf{r}_m - \mathbf{r}_{m+s})/|\mathbf{r}_m - \mathbf{r}_{m+s}|$; positive chirality corresponds to right handed helicity.

The chiral molecule comprising M sites can, thus, be modeled by the Hamiltonian

$$\begin{aligned} \mathcal{H}_{\text{mol}} = & \sum_{m=1}^M \mathcal{H}_m - \sum_{m=1}^{M-1} (\psi_{mn}^\dagger \mathbf{t}_{mnn'} \psi_{(m+1)n'} + H.c.) \\ & + \sum_{m=1}^{M-2} (i\lambda_{mnn'} \psi_{mn}^\dagger \mathbf{v}_m^{(+)} \cdot \sigma \psi_{(m+2)n'} + H.c.), \end{aligned} \quad (16)$$

The molecule is coupled to metallic leads by tunneling interactions

$$\mathcal{H}_T = \sum_p t_p \psi_p^\dagger \psi_1 + \sum_q t_q \psi_q^\dagger \psi_M + H.c., \quad (17)$$

where the leads are modeled by $\mathcal{H}_\chi = \sum_{k \in \chi} \psi_k^\dagger \varepsilon_k \psi_k$, $\varepsilon_k = \varepsilon_k \sigma^0 + \Delta_\chi \sigma^z/2$. Here, $\chi = L, R$ denotes the left (L , $\mathbf{k} = \mathbf{p}$)

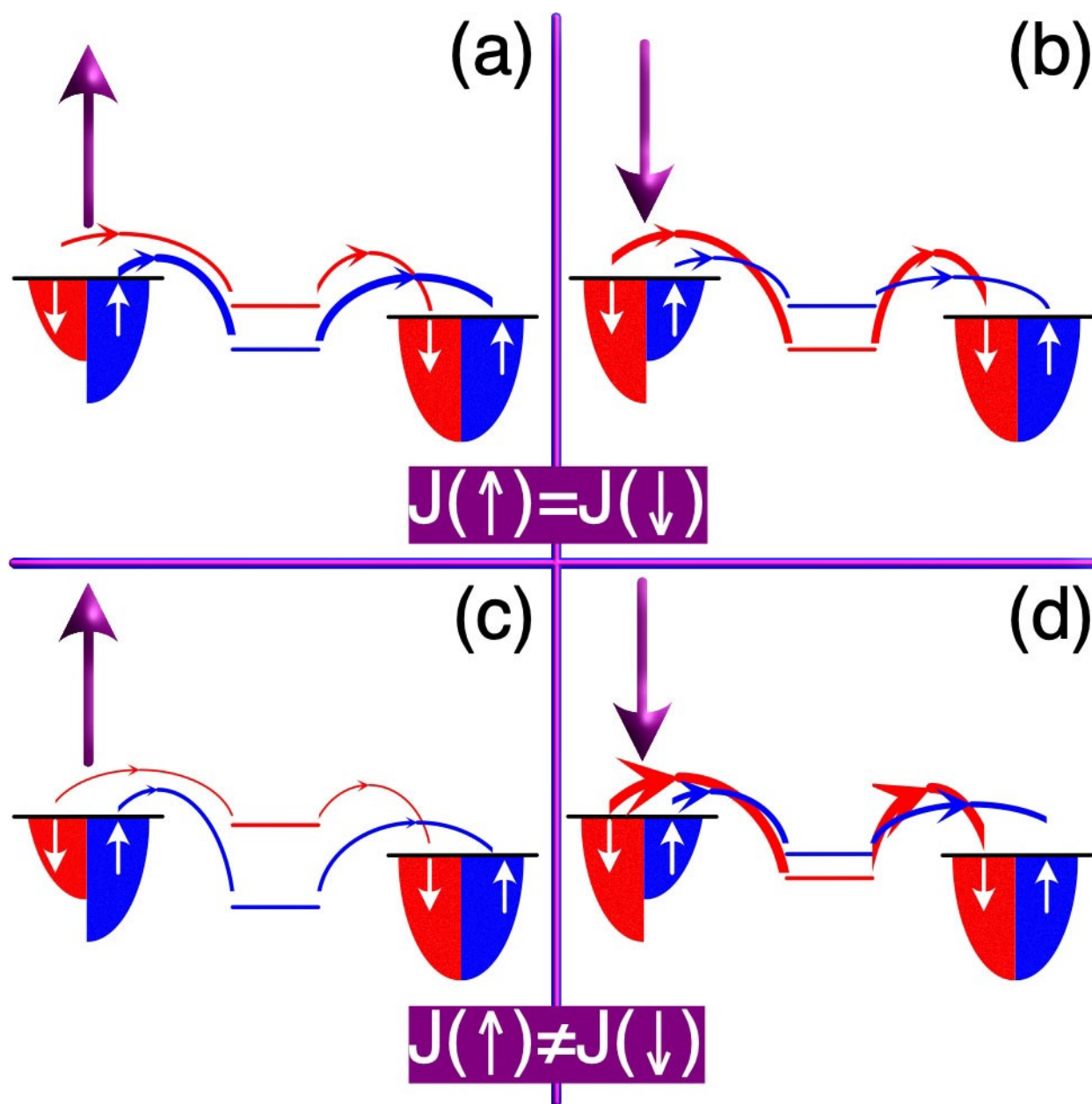


Figure 7. Schematic illustration of how a single particle theory (upper) versus a correlated theory (lower) accounts for the chiral induced spin selectivity effect. The arrow in the upper left corner in each panel signifies the configuration of the external conditions, here, is represented by a ferromagnetic metal in the left lead. The presence of the ferromagnet spin splits the local molecular level. In the single particle theory, this splitting is nominally the same for both types of ferromagnets, however, with opposite signs, see panels (a), (b). The spin-polarizations of the currents in the two cases are equally strong but with the opposite signs, hence, the total charge current remains the same. In a correlated theory, there is a local spin anisotropy which competes with the influence from the ferromagnet, such that the local spin splitting is much large in one configuration compared to the other, see panels (c), (d). This leads to a difference in the total charge current.

or right (R , $\mathbf{k} = \mathbf{q}$) lead, and Δ_χ denotes the spin-gap in the lead. Hence, the full metal-molecule-metal junction is described by

$$\mathcal{H} = \mathcal{H}_L + \mathcal{H}_R + \mathcal{H}_{\text{mol}} + \mathcal{H}_T.$$

The current is calculated using the formula in Eq. (1), which can be obtained by employing standard methods for non-equilibrium Green function, see, e.g., Refs. [59,62]. Specifically, from the Hamiltonian given in Eq. (18), the retarded Green function for the molecule, $G^r(\omega) = \{\mathbf{G}_{mn}^r\}_{mn}$, where $\mathbf{G}_{mn}^r(\omega) = ((\psi_m|\psi_n^\dagger))(\omega + i\delta)$, $\delta > 0$ infinitesimal, is obtained from the expression

$$G^r(\omega) = (\omega - \mathcal{H}_{\text{mol}} + \frac{i}{2}\Gamma)^{-1}, \quad (19)$$

where $\Gamma = \{\Gamma_{mn}\}_{mn}$ is the $M \times M$ -matrix in which all entries are themselves 2×2 -matrices, all zero except $\Gamma_{11} = \Gamma^L$ and $\Gamma_{MM} = \Gamma^R$. The lesser/greater Green functions $G^{</>}$ are provided from the standard relation $G^{</>}(\omega) = (\pm i)\Sigma_{\chi} f_{\chi}(\pm\omega) G^r(\omega) \Gamma G^a(\omega)$, which subsequently are inserted into the expression for the current given in Eq. (1).

2.3.1 Single Electron Per Site

First, consider a single stranded helix, comprising a single electron level per site, that is, $n=1$ for each m . Such a system can be represented in terms of the model introduced in Eqs. (15)–(18) by setting the intra-site hybridization matrix $\mathbf{w}_{mnn'} = 0$, while putting the nearest neighbor and next-nearest neighbor tunneling matrices $\mathbf{t}_{mnn'} = t_0 \sigma^0$ and $\lambda_{mnn'} \mathbf{v}_m^{(s)} \cdot \sigma = \lambda_0 \mathbf{v}_m^{(s)} \cdot \sigma$, assuming uniform tunneling rate throughout the structure. The last assumption is not necessary in the context of single stranded helices, however, it is implemented here for simplicity. For a chain of equivalent sites, it is, furthermore, justified to assume that $\varepsilon_m = \varepsilon = \varepsilon_0 \sigma^0 + \varepsilon_1 \cdot \sigma$. For the sake of illustrating the effect, it is instructive to express the internal spin-anisotropy in terms of an equivalent magnetic field B , such that $\varepsilon_1 = g\mu_B B$, where $g=2$ is the gyromagnetic ratio and μ_B is the Bohr magneton. Then, using $t_0 = 1$ eV, and setting $\lambda_0 = t_0/1,000$, $\Gamma_0 = t_0/10$, $p_L = \pm 0.2\hat{z}$, and $\varepsilon_0 - \mu = -t_0/2$, where μ is the common equilibrium chemical potential of the system, and performing the simulations at $T=300$ K, the resulting normalized magneto-current is shown in Figure 8 (a) for $B=0$ (black), $B=100$ T (blue), $B=500$ T (red), $B=1,000$ T (magenta), and $B=1,500$ T (purple).

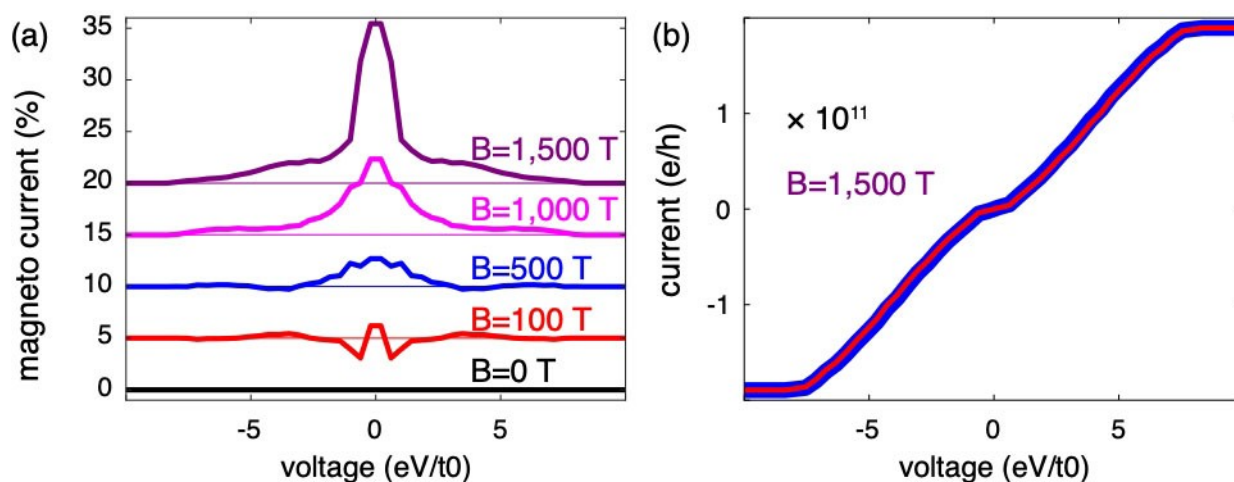


Figure 8. (a) Normalized magneto-current for a 10×6 sites helix as function of the voltage bias for different spin-gaps $\varepsilon^{(1)} = g\mu_B B$, and $B=0$ (black), $B=100$ T (red), $B=500$ T (blue), $B=1,000$ T (magenta), and $B=1,500$ T (purple). Notice that the curves are off-set for clarity. (b) Charge currents for the set-up with $B=1,500$ T. Parameters used are: $\varepsilon_0 - \mu = -1/2$, $\lambda_0 = 1/1,000$, $\Gamma_0 = 1/10$ in units of $t_0 = 1$ eV, and $p_L = \pm 0.2\hat{z}$ at $T=300$ K.

500 T (purple). The currents for $p_L = 0.2\hat{z}$ (blue) and $p_L = -0.2\hat{z}$ (red) in Figure 8 (b), correspond to the case $B=1,500$ T.

As can be expected, there is no magneto-current in absence of the spin anisotropy (black), while it increases with increasing B . In the light of experimental observations where magneto-currents between a few percent to nearly a hundred percent, the values of the normalized magneto-currents plotted in Figure 8 are reasonable. However, while the magnitudes of the equivalent B -fields are unrealistically large, they illustrate the inability to represent and explain the chiral induced spin selectivity effect in single stranded helices in terms of single electron theory using realistic values on the parameters. Despite this inability, the observation that the chiral induced spin selectivity effect actually can be obtained by inclusion of the spin anisotropy ε_1 , suggests that it should be possible to address the effect through electron correlations, as was previously done in, e.g., Refs. [59,61–66].

2.3.2 Multiple Electrons Per Site

It has been argued that while the single stranded helix cannot be effectively modelled to provide a non-vanishing chiral induced spin selectivity effect,^[39–41,50] this should be possible in a double stranded helix. Hence, whereas the example above can be regarded as to represent a single stranded helix, a double, or multiple, stranded helix can be represented in terms of the full model introduced in Eqs. (15)–(18), by letting the intra-site and inter-site hybridization matrices $\mathbf{w}_{mnn'}$, and $\mathbf{t}_{mnn'}$, respectively, assume non-zero values, with $n=1, 2, \dots$ for each m . Hence, transitions from all n to all n' are allowed. For simplicity, however, it is assumed that $\mathbf{w}_{mnn'} = w_0 \sigma^0 + \mathbf{w}_1 \cdot \sigma$, $\mathbf{t}_{mnn'} = t_0 \sigma^0 + \mathbf{t}_1 \cdot \sigma$, and $\lambda_{mnn'} = \lambda_0$, that is, again assuming

uniform hybridization rates throughout the structure. The values from the single stranded structure are retained, that is, $t_0 = 1$ eV, $\lambda_0 = t_0/1,000$, and $\Gamma_0 = t_0/10$.

Regarding the model to represent a double stranded helix with a single level per site, or a single stranded helix with two energy levels per site, it is first assumed that the energy levels are degenerate, such that $\varepsilon = \varepsilon^{(0)}\sigma^0$, and setting $\varepsilon^{(0)} - \mu = \varepsilon - \mu = -t/2$, for all m and n . In Figure 9, the magneto-currents are plotted as function of the voltage bias for a 2×3 with two degenerate energy levels per m with (a) $w_1/w_0 = (0,0,0)$, (b) $w_1/w_0 = (0,0,0.1)$, (c) $w_1/w_0 = (1,1,0)$, and (d) $w_1/w_0 = (1,1,0.1)$, and inter-site tunneling (green) $t_1/t_0 = (0,0,0)$, (blue) $t_1/t_0 = (1,1,0)$, (red) $t_1/t_0 = (1,1,0.001)$, and (purple) $t_1/t_0 = (0,0,0.001)$, and $w_0 = -1/100$ in units of $t_0 = 1$ eV, while other parameters are as in Figure 8.

Under all conditions but one, there is a non-vanishing magneto-current, however, in all cases it is less than 0.3%.

Absence of spin-dependent hybridization, that is, both $w_{mn\sigma} = w_0\sigma^0$ and $t_{mn\sigma} = t_0\sigma^0$, yields a magneto-current which vanishes identically, see Figure 9 (a) (green). In all cases, the next-nearest neighbor spin-orbit coupling $\lambda_{mn\sigma} \neq 0$. Hence, these results point towards an important aspect of the chiral structures. Namely, the mixing of the electronic structures of two separate helices, such that, at least one of $w_{mn\sigma}^{(1)}$ and $t_{mn\sigma}^{(1)}$ are non-vanishing, introduces an intrinsic spin anisotropy in the structure which clearly is not there in the complete absence of this mixing. In this sense, then, these results corroborate the conclusions drawn in Refs. [39–41,50], that a double stranded structure is necessary to obtain the effect. However, these results also suggest that the magneto-current is likely to be less than a percent in a set-up with realistic values. The conclusions drawn in Refs. [39,40,50] should be related to the inclusion of a dissipative contribution, something which would generate a large chiral induced spin selectivity effect, which also corroborates the conclusions from Refs. [59,61–66].

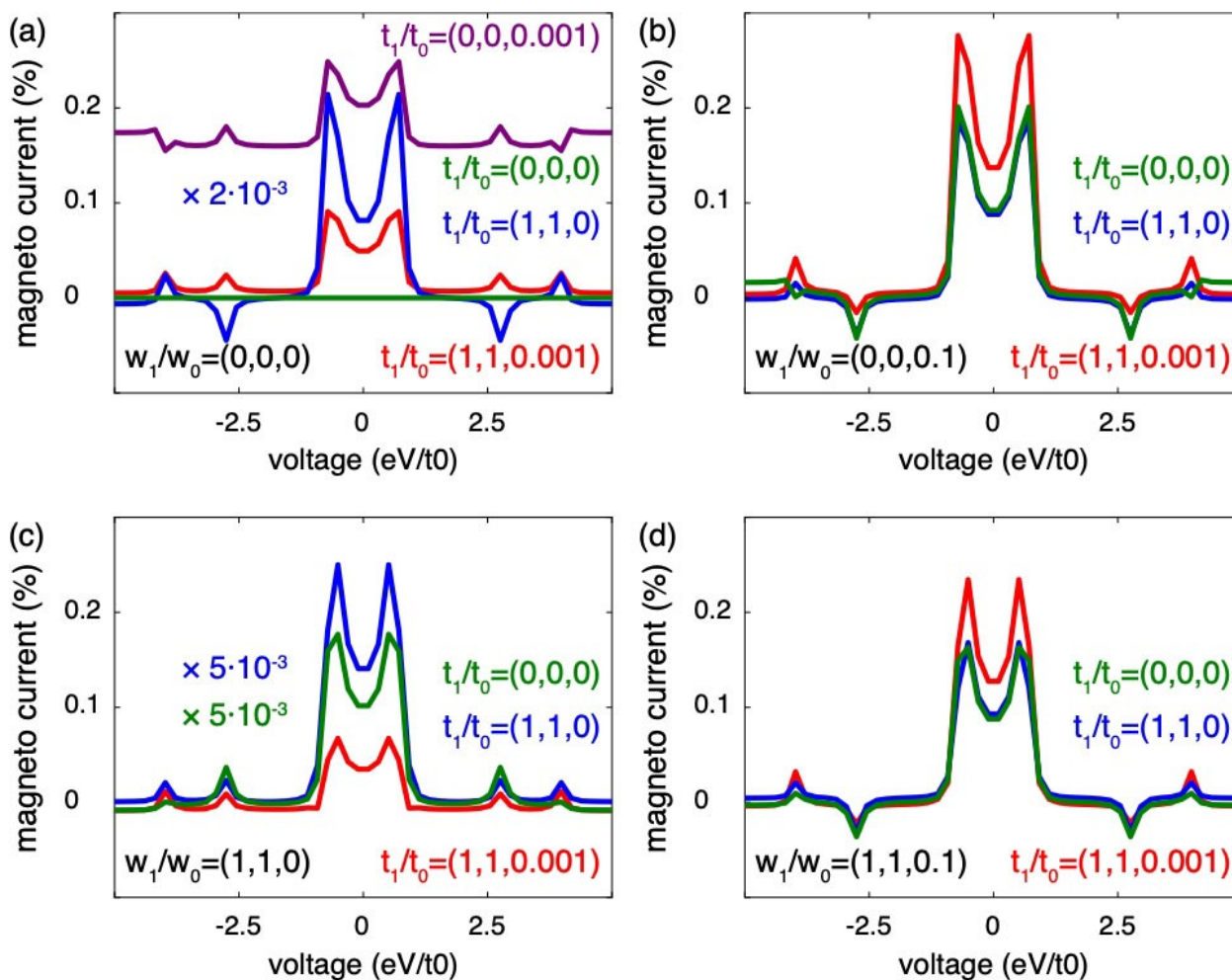


Figure 9. Normalized magneto-current for a 2×3 sites helix with two energy levels per site, for different intra-site and inter-site level hybridizations w_1 and t_1 , respectively. (a) $w_1/w_0 = 0$, (b) $w_1/w_0 = (0,0,1/10)$, (c) $w_1/w_0 = (1,1,0)$, and (d) $w_1/w_0 = (1,1,1/10)$, where $t_1/t_0 = (1,1,1/1,000)$ (red); $t_1/t_0 = (1,1,0)$ (blue); $t_1/t_0 = 0$ (green); $t_1/t_0 = (0,0,1/1,000)$ (purple). Parameters used are: $\varepsilon_0 - \mu = -1/2$, $\lambda_0 = 1/1,000$, $\Gamma_0 = 1/10$ in units of $t_0 = 1$ eV, and $p_L = \pm 0.2\hat{z}$ at $T = 300$ K.

It should, moreover, be noticed in the results presented in Figure 9, that a sole transverse spin-dependent mixing $t_{mm'}^{(1)}$ results in a non-vanishing magneto-current, see Figure 9 (blue). Despite this observation, it should also be noticed that the magneto-current is strongly suppressed in the absence of a longitudinal mixing. Hence, by introducing a longitudinal spin mixing component to either of $w_{mm'}^{(1)}$ or $t_{mm'}^{(1)}$ enhances the magneto-current by about three orders of magnitude. The picture remains qualitatively unchanged when lifting the degeneracy of the energy levels $\varepsilon_{mm}^{(0)}$, letting, for instance, $\varepsilon_{m1}^{(0)} < \varepsilon_{m2}^{(0)} < \dots$. The simulated results for a 2×3 molecule with $\varepsilon_{m1}^{(0)} - \mu = -2t_0$ and $\varepsilon_{m2}^{(0)} - \mu = -t_0/2$ are summarized in Figure 10 (a) $w_1/w_0 = (0, 0, 0)$, (b) $w_1/w_0 = (0, 0, 1/10)$, and (c) $w_1/w_0 = (1, 1, 0)$, with (green) $t_1/t_0 = (0, 0, 0)$, (blue) $t_1/t_0 = (1, 1, 0)$, (red) $t_1/t_0 = (1, 1, 0.001)$, and (purple) $t_1/t_0 = (0, 0, 0.001)$, and $w_0 = -1/100$ in units of $t_0 = 1$ eV, while other parameters are as in Figure 8.

The lowered symmetry of the molecule is reflected in more details in the magneto-current, however, the overall amplitude of the magneto-current is reduced to less than 0.1 %. This reduction in the amplitude can be understood as a reflection of the lowered symmetry, which leads to less resonant states in the structure and, hence, a weaker intrinsic spin anisotropy. Introducing more (non-degenerate) energy levels, equidistantly distributed in the energy range between $-2t_0$ and $-t_0/2$, Figure 10 (d) (blue) two levels, (red) three levels, (purple) four levels, and (green) five levels, facilitates an enhancement of the magneto-current. This enhancement can be attributed to (i) the increasing number of conduction channels and (ii) the lowered spacing between adjacent energy levels, both conditions which increase the symmetry of the spectrum in the sense that more and more states become nearly resonant which, in turn, increases the intrinsic spin anisotropy.

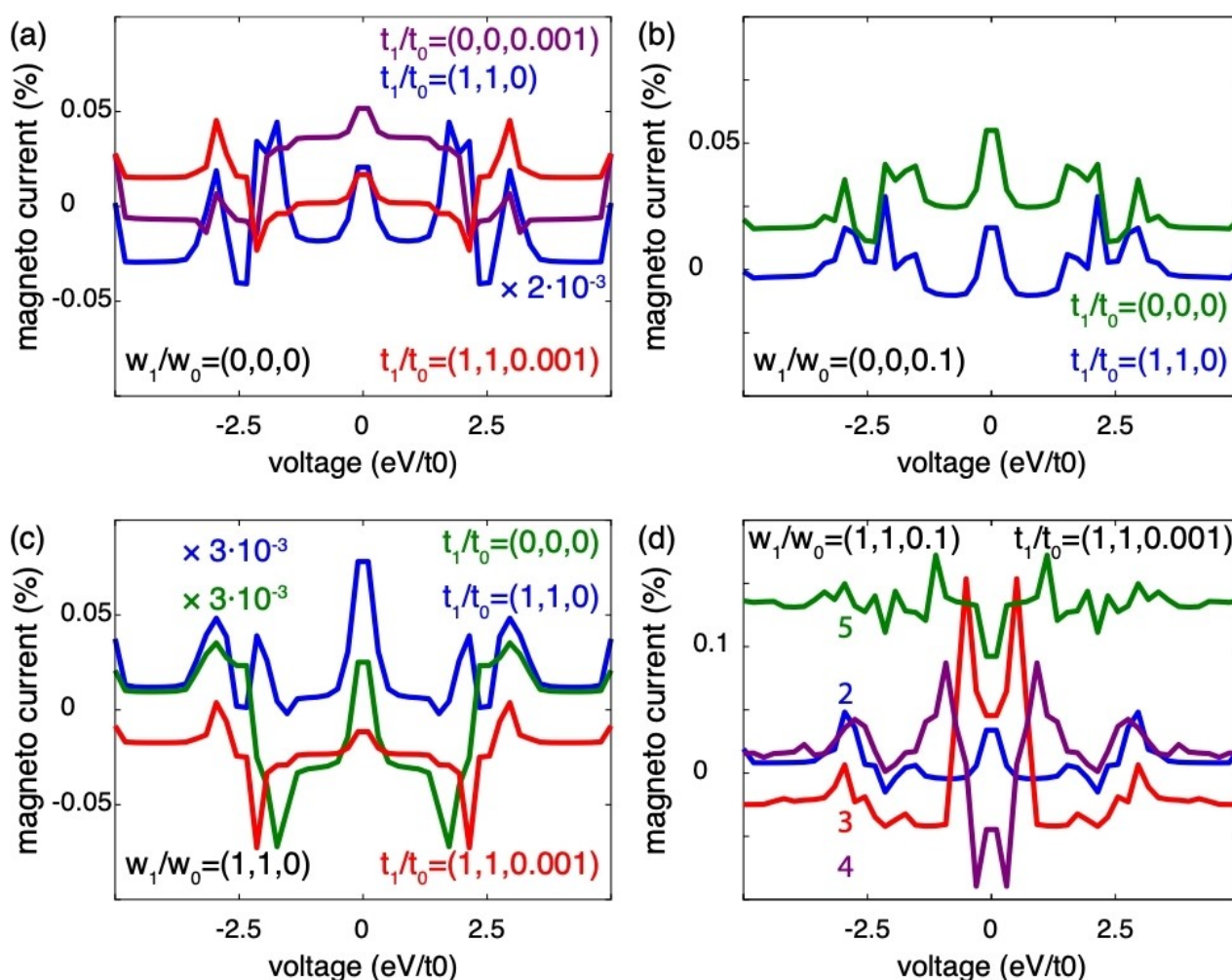


Figure 10. Normalized magneto-current for a 2×3 sites helix with two energy levels per site, for different intra-site and inter-site level hybridizations w_1 and t_1 , respectively. (a) $w_1/w_0 = 0$, (b) $w_1/w_0 = (0, 0, 0.1)$, (c) $w_1/w_0 = (1, 1, 0)$, and (d) $w_1/w_0 = (1, 1, 0.1)$, where $t_1/t_0 = (1, 1, 0.001)$ (red); $t_1/t_0 = (1, 1, 0)$ (blue); $t_1/t_0 = 0$ (green); $t_1/t_0 = (0, 0, 0.001)$ (purple). Parameters used are: $\varepsilon_0 - \mu = -0.5$, $\lambda_0 = 0.001$, $T_0 = 0.1$ in units of $t_0 = 1$ eV, and $\varepsilon_1 = g\mu_B B$, $B = 500$ T and $p_L = \pm 0.2z$ at $T = 300$ K.

In all the examples presented and discussed here, the amplitude of the normalized magneto-current is less than one percent, and it is worth to elaborate on reasons why this is the case. First, the chiral induced spin selectivity effect is not a measure of the induced spin-polarization in the molecule, or, in the composite system comprising the molecule and the leads, due to the spin-polarization of the injected electrons. The chiral induced spin selectivity effect is a measure of the variations of the charge current as function of the magnetic conditions applied to the system. The difference between the two concepts can be understood as the difference between the charge and spin currents, where only the former is directly related to the chiral induced spin selectivity effect.

3. Conclusions

In conclusion, it has been shown that when comparing theoretical results with measurements of the chiral induced spin selectivity effect, one inevitably has to study the charge currents obtained for different configurations of the externally applied spin-polarization or magnetic field. For such comparisons, the spin-polarized transmission of the system has little, if anything, to do with the conclusions one can draw about the effect for different compounds and configurations of the setup. Likewise, while the spin-current may be used to extract deeper information about the origin of the chiral induced spin selectivity, thus far, there is no such experimental result with which the spin-current can be compared. It is, therefore, an important observation that studies of the chiral induced spin selectivity in terms of the spin-polarized current or the spin current lead to conclusions that cannot be directly compared to any of the experimental observations reported thus far. Reported observations of the chiral induced spin selectivity effect only concerns the properties that can be related to the charge currents. It has, furthermore, been demonstrated that while single-electron models, in general, are not viable tools to describe the chiral induced spin selectivity effect, by introducing an effective spin anisotropy to the molecular junction one can, nonetheless, construct simple models as fitting tools. However, these effective spin anisotropies typically correspond to unrealistically large magnetic fields, which make the usefulness of such constructions questionable. Moreover, the origin of such spin anisotropies is related to the interplay between the structure, spin-orbit interactions, and electron correlations. The effective spin anisotropy can, in this sense, be thought of as a parametrization of the electron correlations. Finally, it was demonstrated that while the chiral induces spin selectivity effect can be enhanced by introducing more channels which are spin-dependently interconnected, the enhancement of the effect is still marginal, resulting in effects that are less than 1% in models using somewhat realistic parameter values.

This should conclude the discussion of the potential usefulness of single electron models for the description of the chiral induced spin selectivity effect, as well as to why the

spin-resolved transmissions should not be used in comparison with the experimental observations of the effect.

Acknowledgements

The author thanks R. Naaman and Y. Dubi for constructive and fruitful discussions. This work was supported by Vetenskapsrådet and Stiftelsen Olle Engkvist Byggmästare.

Data Availability Statement

Data sharing is not applicable to this article as no new data were created or analyzed in this study.

References

- [1] K. Ray, S. P. Ananthavel, D. H. Waldeck, R. Naaman, *Science* **1999**, 283, 814–816.
- [2] B. Göhler, V. Hamelbeck, T. Z. Markus, M. Kettner, G. F. Hanne, Z. Vager, R. Naaman, H. Zacharias, *Science* **2010**, 331, 894–897.
- [3] D. H. Waldeck, R. Naaman, Y. Paltiel, *APL Mater.* **2021**, 9, 040902.
- [4] D. Mishra, T. Z. Markus, R. Naaman, M. Kettner, B. Göhler, H. Zacharias, N. Friedman, M. Sheves, C. Fontanesi, *Proc. Natl. Acad. Soc.* **2013**, 110, 14872–14876.
- [5] M. Eckshtain-Levi, E. Capua, S. Refaely-Abramson, S. Sarkar, Y. Gavrilov, S. P. Mathew, Y. Paltiel, Y. Levy, L. Kronik, R. Naaman, *Nat. Commun.* **2016**, 7, 10744.
- [6] C. Fontanesi, E. Capua, Y. Paltiel, D. H. Waldeck, R. Naaman, *Adv. Mater.* **2018**, 30, 1707390.
- [7] O. B. Dor, N. Morali, S. Yochelis, L. T. Baczewski, Y. Paltiel, *Nano Lett.* **2014**, 14, 6042–6049.
- [8] P. C. Mondal, P. Roy, D. Kim, E. E. Fullerton, H. Cohen, R. Naaman, *Nano Lett.* **2016**, 16, 2806–2811.
- [9] P. Roy, N. Kantor-Uriel, D. Mishra, S. Dutta, N. Friedman, M. Sheves, R. Naaman, *ACS Nano* **2016**, 10, 4525–4531.
- [10] J. M. Abendroth, N. Nakatsuka, M. Ye, D. Kim, E. E. Fullerton, A. M. Andrews, P. S. Weiss, *ACS Nano* **2017**, 11, 7516–7526.
- [11] M. Kettner, V. V. Maslyuk, D. Nürenberg, J. Seibel, R. Gutierrez, G. Cuniberti, K.-H. Ernst, H. Zacharias, *J. Phys. Chem. Lett.* **2018**, 9, 2025–2030.
- [12] K. Banerjee-Ghosh, O. B. Dor, F. Tassinari, E. Capua, S. Yochelis, A. Capua, S.-H. Yang, S. S. P. Parkin, S. Sarkar, L. Kronik, L. T. Baczewski, R. Naaman, Y. Paltiel, *Science* **2018**, 360, 1331–1334.
- [13] J. M. Abendroth, K. M. Cheung, D. M. Stemer, M. S. El Hadri, C. Zhao, E. E. Fullerton, P. S. Weiss, *J. Am. Chem. Soc.* **2019**, 141, 3863–3874.
- [14] D. M. Stemer, J. M. Abendroth, K. M. Cheung, M. Ye, M. S. El Hadri, E. E. Fullerton, P. S. Weiss, *Nano Lett.* **2020**, 20, 1218–1225.
- [15] Z. Huang, B. P. Bloom, X. Ni, Z. N. Georgieva, M. Marciesky, E. Vetter, F. Liu, D. H. Waldeck, D. Sun, *ACS Nano* **2020**, 14, 10370–10375.
- [16] Y. Sang, S. Mishra, F. Tassinari, S. K. Karuppannan, R. Carmieli, R. D. Teo, A. Migliore, D. N. Beratan, H. B. Gray, I. Pecht, J.

- Fransson, D. H. Waldeck, R. Naaman, *J. Phys. Chem. C* **2021**, *125*, 9875–9883.
- [17] I. Meirzada, N. Sukenik, G. Haim, S. Yochelis, L. T. Baczewski, Y. Paltiel, N. Bar-Gill, *ACS Nano* **2021**, *15*, 5574–5579.
- [18] P. V. Möllers, S. Ulku, D. Jayarathna, F. Tassinari, D. Nürenberg, R. Naaman, C. Achim, H. Zacharias, *Chirality* **2021**, *33*, 93.
- [19] Z. Xie, T. Z. Markus, S. R. Cohen, Z. Vager, R. Gutierrez, R. Naaman, *Nano Lett.* **2011**, *11*, 4652–4655.
- [20] S. Ghosh, S. Mishra, E. Avigad, B. P. Bloom, L. T. Baczewski, S. Yochelis, Y. Paltiel, R. Naaman, D. H. Waldeck, *J. Phys. Chem. Lett.* **2020**, *11*, 1550–1557.
- [21] V. Kiran, S. P. Mathew, S. R. Cohen, I. H. Delgado, J. Lacour, R. Naaman, *Adv. Mater.* **2016**, *28*, 1957–1962.
- [22] H. Alpern, K. Yavilberg, T. Dvir, N. Sukenik, M. Klang, S. Yochelis, H. Cohen, E. Grosfeld, H. Steinberg, Y. Paltiel, O. Millo, *Nano Lett.* **2019**, *19*, 5167–5175.
- [23] A. K. Mondal, N. Brown, S. Mishra, P. Makam, D. Wing, S. Gilead, Y. Wiesenfeld, G. Leitun, L. J. W. Shimon, R. Carmieli, D. Ehre, G. Kamieniarz, J. Fransson, O. Hod, L. Kronik, E. Gazit, R. Naaman, *ACS Nano* **2020**, *14*, 16624–16633.
- [24] E. Z. B. Smolinsky, A. Neubauer, A. Kumar, S. Yochelis, E. Capua, R. Carmieli, Y. Paltiel, R. Naaman, K. Michaeli, *J. Phys. Chem. Lett.* **2019**, *10*, 1139–1145.
- [25] O. B. Dor, S. Yochelis, S. P. Mathew, R. Naaman, Y. Paltiel, *Nat. Commun.* **2013**, *4*, 2256.
- [26] O. B. Dor, S. Yochelis, A. Radko, K. Vankayala, E. Capua, A. Capua, S.-H. Yang, L. T. Baczewski, S. S. P. Parkin, R. Naaman, Y. Paltiel, *Nat. Commun.* **2016**, *8*, 14567.
- [27] A. Inui, R. Aoki, Y. Nishiue, K. Shiota, Y. Kousaka, H. Shishido, D. Hirobe, M. Suda, J. Ohe, J. Kishine, H. M. Yamamoto, Y. Togawa, *Phys. Rev. Lett.* **2021**, *124*, 166602.
- [28] K. Shiota, A. Inui, Y. Hosaka, R. Amano, Y. Ōnuki, M. Hedo, T. Nakama, D. Hirobe, J. Ohe, J. Kishine, H. M. Yamamoto, H. Shishido, Y. Togawa, *Phys. Rev. Lett.* **2021**, *127*, 126602.
- [29] S. Yeganeh, M. A. Ratner, E. Medina, V. Mujica, *J. Chem. Phys.* **2009**, *131*, 014707.
- [30] E. Medina, F. López, M. A. Ratner, V. Mujica, *EPL* **2012**, *99*, 17006.
- [31] S. Varela, E. Medina, F. López, V. Mujica, *J. Phys. Condens. Matter* **2013**, *26*, 015008.
- [32] A. A. Eremko, V. M. Loktev, *Phys. Rev. B* **2013**, *88*, 165409.
- [33] E. Medina, L. A. González-Arraga, D. Finkelstein-Shapiro, B. Berche, V. Mujica, *J. Chem. Phys.* **2015**, *142*, 194308.
- [34] E. Díaz, A. Conteras, J. Hernández, F. Domínguez-Adame, *Phys. Rev. E* **2018**, *98*, 052221.
- [35] X. Yang, C. H. van der Wal, B. J. van Wees, *Phys. Rev. B* **2019**, *99*, 024418.
- [36] E. Díaz, P. Albares, P. G. Estévez, J. M. Cerveró, C. Gaul, E. Diez, F. Domínguez-Adame, *New J. Phys.* **2018**, *20*, 043055.
- [37] K. Michaeli, R. Naaman, *J. Phys. Chem. C* **2019**, *123*, 17043–17048.
- [38] R. Gutierrez, E. Díaz, R. Naaman, G. Cuniberti, *Phys. Rev. B* **2012**, *85*, 081404(R).
- [39] A.-M. Guo, Q.-F. Sun, *Phys. Rev. Lett.* **2012**, *108*, 218102.
- [40] A.-M. Guo, A.-F. Sun, *Proc. Natl. Acad. Soc.* **2014**, *11*, 11658–11662.
- [41] Y. Utsumi, O. Entin-Wohlman, A. Aharony, *Phys. Rev. B* **2020**, *102*, 035445.
- [42] D. Rai, M. Galperin, *J. Phys. Chem. C* **2013**, *117*, 13730–13737.
- [43] S. Matityahu, Y. Utsumi, A. Aharony, O. Entin-Wohlman, C. A. Balseiro, *Phys. Rev. B* **2016**, *93*, 075407.
- [44] S. Varela, V. Mujica, E. Medina, *Phys. Rev. B* **2016**, *93*, 155436.
- [45] S. Behnia, S. Fathizadeh, A. Akhshani, *Chem. Phys.* **2016**, *477*, 61–73.
- [46] V. V. Maslyuk, R. Gutierrez, A. Dianat, V. Mujica, G. Cuniberti, *J. Phys. Chem. Lett.* **2018**, *9*, 5453–5459.
- [47] E. Díaz, F. Domínguez-Adame, R. Gutierrez, G. Cuniberti, V. Mujica, *J. Phys. Chem. Lett.* **2018**, *9*, 5753–5758.
- [48] M. S. Zöllner, S. Varela, E. Medina, V. Mujica, C. Herrmann, *J. Chem. Theory Comput.* **2020**, *16*, 2914–2929.
- [49] A. Ghazaryan, M. Lemesheko, A. G. Volosniev, *Commun. Phys.* **2020**, *3*, 178.
- [50] A. Shitade, E. Minamitani, *New J. Phys.* **2020**, *22*, 113023.
- [51] G.-H. Du, H.-H. Fu, R. Wu, *Phys. Rev. B* **2020**, *102*, 035431.
- [52] T. P. Fay, D. T. Limmer, *Nano Lett.* **2021**, *21*, 6696–6702.
- [53] C. Wang, A.-M. Guo, Q.-F. Sun, Y. Yan, *J. Phys. Chem. Lett.* **2021**, *12*, 10262–10269.
- [54] C. Z. Wang, V. Mujica, Y.-C. Lai, *Nano Lett.* **2021**, *21*, 10423–10430.
- [55] X. Bian, Y. Yanze Wu, H.-H. Teh, Z. Zhou, J. E. Subotnik, *J. Chem. Phys.* **2021**, *154*, 110901.
- [56] A. G. Volosniev, H. Alpern, Y. Paltiel, O. Millo, M. Lemesheko, A. Ghazaryan, *Phys. Rev. B* **2021**, *104*, 024430.
- [57] D. A. Hoff, L. G. C. Rego, *Nano Lett.* **2021**, *21*, 8190–8196.
- [58] S. Dalum, P. Hedegård, *Nano Lett.* **2019**, *19*, 5253–5259.
- [59] J. Fransson, *J. Phys. Chem. Lett.* **2019**, *10*, 7126–7132.
- [60] A. Dianat, R. Gutierrez, H. Alpern, V. Mujica, A. Ziv, S. Yochelis, O. Millo, Y. Paltiel, G. Cuniberti, *Nano Lett.* **2020**, *20*, 7077–7086.
- [61] L. Zhang, Y. Hao, W. Qin, S. Xie, F. Qu, *Phys. Rev. B* **2020**, *102*, 214303.
- [62] J. Fransson, *Phys. Rev. B* **2020**, *102*, 235416.
- [63] J. Fransson, *Nano Lett.* **2021**, *21*, 3026–3032.
- [64] S. Alwan, Y. Dubi, *J. Am. Chem. Soc.* **2021**, *143*, 14235–14241.
- [65] K. H. Huisman, J. M. Thijssen, *J. Phys. Chem. C* **2021**, *125*, 23364–23369.
- [66] J. Fransson, *J. Phys. Chem. Lett.* **2022**, *13*, 808–814.
- [67] H. -H. Teh, W. Dou, J. E. Subotnik, Spin Polarization through A Molecular Junction Based on Nuclear Berry Curvature Effects, **2021**; arXiv:2111.12815.
- [68] Y. Wu, J. E. Subotnik, *J. Chem. Phys.* **2021**, *154*, 234101.
- [69] H.-H. Teh, W. Dou, J. E. Subotnik, *Phys. Rev. B* **2021**, *104*, L201409.
- [70] A. Kato, H. M. Yamamoto, J.-I. Kishine, *Phys. Rev. B*, **2021**, *105*, 195117.
- [71] J. Fransson, *Phys. Rev. B* **2005**, *72*, 075314.
- [72] A.-P. Jauho, N. S. Wingreen, Y. Meir, *Phys. Rev. B* **1994**, *50*, 5528–5544.
- [73] J. Fransson, *Non-Equilibrium Nano-Physics* Springer: Dordrecht, **2010**.
- [74] J. Fransson, *Phys. Rev. B* **2005**, *72*, 045415.

Manuscript received: July 14, 2022
Version of record online: November 27, 2022